AIAA JOURNAL
Vol. 47, No. 2, February 2009

New Two-Equation Closure for Rough-Wall Turbulent Flows Using the Brinkman Equation

Meng-Huang Lu* and William W. Liou†
Western Michigan University, Kalamazoo, Michigan 49008

DOI: 10.2514/1.38404

A new flow-physics-based modeling of surface-roughness effects is developed for the Reynolds-averaged Navier–Stokes equations numerical calculations of high-Reynolds-number turbulent flows over rough walls. In the proposed approach, we model the fluid dynamics of the volume-averaged flow in the near-wall rough layer by using the Brinkman equation. The porosity can be calculated based on the volumetric characteristics of the roughness, and the permeability is modeled. The Reynolds-averaged Navier–Stokes equations are solved numerically above the near-wall rough layer, and a low-Reynolds-number k-ε model is employed in all regions. In this paper, we present the computational results, including the skin-friction coefficient, the log-law mean velocity, the roughness function, the turbulent kinetic energy, and the Reynolds shear stress. The results show that the new rough-wall-layer modeling approach well predicts the skin-friction coefficient, the log-law mean velocity, the roughness function, and the Reynolds shear stress.

Nomenclature

C_f	=	skin-friction coefficient
Da	=	Darcy number
d_P	=	effective diameter
H	=	channel height
K	=	permeability
k	=	turbulent kinetic energy
k_s	=	roughness height
k_{eq}	=	equivalent sand roughness height
L	=	plate length
P	=	pressure
Re	=	Reynolds number
Re_θ	=	Reynolds number based on momentum thickness
R_t	=	turbulence Reynolds number defined as $k^2/\varepsilon\nu$
t	=	time
U_b	=	bulk velocity
U_0	=	freestream velocity
$\langle\bar{u}\rangle$	=	superficial average mean velocity
u_τ	=	friction velocity
ΔU	=	roughness function
ΔV	=	averaging volume
δ	=	boundary-layer thickness
δ_B	=	thickness of the roughness region
ε	=	dissipation rate of the turbulent kinetic energy
ε_β	=	porosity
ν	=	fluid viscosity
ν_t	=	turbulent eddy viscosity
ρ	=	fluid density

Subscripts

β	=	quantity associated with the fluid phase in the roughness region
I	=	quantity associated with the interface

Superscripts

β	=	intrinsic volume average
$+$	=	normalized with inner variables

I. Introduction

NUMERICAL simulations of turbulent boundary layers over rough surfaces present great challenges and interest to many engineering problems [1] such as boundary layers over naval vehicle platforms, flight vehicles, turbomachinery blades, pipes, and heat exchangers. Surface roughness alters the flow structure in the turbulent boundary layer near the wall and causes the increase of drag and wall heat transfer. Direct numerical simulation (DNS), large-eddy simulation (LES), and Reynolds-averaged Navier–Stokes equations (RANS) have been employed to examine the turbulent flows over rough surfaces. There are two commonly used approaches in DNS and LES to simulate the effect of surface roughness. The first approach accounts for the blockage effect of the roughness element on the flow by adding a form-drag term in the momentum equation [2–5]. The coefficient for the form-drag term is determined a priori by examining the corresponding experimental data. The second is the body-force/immersed-boundary method [6–9], in which the no-slip boundary is enforced via a body-force term.

For the numerical calculation using RANS, the averaged effect of surface roughness is modeled. One commonly used approach is adding form-drag terms in the governing equations to account for the roughness effect [10–15]. However, the coefficients in the model formulations for the form drag are flow-specific [10,13,15]. RANS-based calculations have also been performed by using roughness models modified from the existing turbulence models developed for smooth-wall flows. Krogstad [16] modified the damping function of van Driest [17] and calculated the roughness function for large roughness. Youn et al. [18] employed the standard k-ε model with wall function to predict the friction factor valid for Reynolds numbers between 10^5 and 10^7 in the rectangular duct with one side rib-roughened. A method for predicting the friction factor using existing correlations for smooth and rough walls was developed.

A common approach adopted in the numerical modeling of roughness is to relate the roughness effects to an equivalent sand roughness, thereby ignoring any possible dependence of the turbulent flow structure on the specific surface geometry. Zhang et al. [19] proposed a low-Reynolds-number k-ε model to simulate turbulent flow over smooth and rough surfaces by including the equivalent sand roughness k_{eq}^+ into the damping functions of van Driest [17] and Lam and Bremhorst [20]. The predictions of skin-friction coefficient and log-law velocity shift showed good

Presented as Paper 0649 at the 46th AIAA Aerospace Sciences Meeting and Exhibit, Reno, NV, 7–10 January 2008; received 5 May 2008; revision received 5 September 2008; accepted for publication 22 September 2008. Copyright © 2008 by the authors. Published by the American Institute of Aeronautics and Astronautics, Inc., with permission. Copies of this paper may be made for personal or internal use, on condition that the copier pay the $10.00 per-copy fee to the Copyright Clearance Center, Inc., 222 Rosewood Drive, Danvers, MA 01923; include the code 0001-1452/09 $10.00 in correspondence with the CCC.

*Research Associate, Mechanical and Aeronautical Engineering.
†Professor, Mechanical and Aeronautical Engineering. Associate Fellow AIAA.

agreement with the experimental measurements of fully developed rough pipe and duct flows of Reynolds numbers between 5×10^3 and 5×10^7 and the equivalent sand roughness k_{eq}^+ from 0 up to 1000. Durbin et al. [21] added a hydrodynamic roughness length for the two-layer k-ε turbulence model of Chen and Patel [22] for a sand-grain roughness surface. The model was used to calculate the flat-plate boundary layer subjected to freestream acceleration and backward-facing ramp flows. Foti and Scandura [23] developed a low-Reynolds-number k-ε model for oscillatory flows over smooth and rough surfaces based on the model of Lam and Bremhorst [20]. The results showed that the model predicted the wall stresses, velocity profile, and boundary-layer thickness. However, the implementation of this model requires the equivalent sand roughness k_{eq}^+ as a model input parameter, which is best determined using experimental data measured in the same flow. In light of the practical importance of the surface-roughness effects in many engineering problems, there is an apparent need to develop predictive modeling for the RANS type of calculations for turbulent flows over roughness.

In this paper, a new modeling approach for the wall roughness effect is presented. The model explicitly recognizes the inhomogeneous nature of the media (i.e., solid and fluid) in the roughness region. The dynamics of the fluid flow are filtered through volume averaging, which gives rise to the Brinkman equation frequently used in the study of flow through porous media. The geometry and the formation of the surface roughness are accounted for through porosity that can be calculated mathematically and through permeability. The proposed exploratory use of the Brinkman equation is innovative, because this widely used approach in porous-medium flow calculations has never been applied to the modeling of the rough-wall effects on high-Reynolds-number flows.

Without losing generality, in the implementation described in this paper, the turbulence closure is provided by developing a low-Reynolds-number k-ε model based on a turbulence model [24] that is widely implemented in many RANS solvers. In the following, the modeling approach, the mathematical formulation, and the numerical framework will be described. The implementation of the baseline low-Reynolds-number k-ε model of Launder and Sharma [24] is first evaluated by comparing the calculated fully developed turbulent smooth channel flows and smooth-wall turbulent boundary layers with DNS data [25] and experimental measurements [26]. The proposed new rough-wall-layer modeling using the Brinkman equation is then examined by simulating fully developed turbulent channel and boundary-layer flows over different types of roughness. They include the turbulent rough channel flows with the square rod and the mesh roughness measured by Bakken et al. [27] with the Reynolds numbers, based on the channel height, of 60,000 and 62,000, respectively. Rough-wall turbulent boundary layers with surface roughnesses of woven mesh [28,29], cylinder [30], square rod [31], and perforated plate [32] have also been calculated. The momentum-thickness Reynolds number for these flows ranges from 4000 to about 14,000. These cases have been used to assess the present model, as the roughness geometries are well defined and the flows are considered fully rough, based on the reported roughness Reynolds number k_s^+ ranging between 83 and 150. The calculated results of the skin-friction coefficient, the mean flow velocity, the roughness function, the Reynolds shear stress, and the turbulent kinetic energy are compared with the corresponding experimental measurements.

II. Modeling Approach

For a turbulent boundary layer flowing over a rough wall, the fluid is diverted around the roughness elements due to the blockage effect of the roughness. It can then be argued that one can view the boundary layer as being made up of two regions. The first is the near-wall region in which the fluid flow is perturbed by the surface roughness. The second is a free-flow region in the core part of the boundary layer. In the roughness near-wall layer, the flow is essentially being forced to move through spaces that are partially blocked and partially free to go through. A similar scenario can be found in porous-medium flows, in which the fluid flows through pores and openings. Other than the geometric similarities, the two flows are both viscous-dominated due to the large wetted area with embedded regions of shear, and the local Reynolds number tends to be low. The geometric and the dynamic similarities between these two types of flows are important. It naturally leads to a hypothesis that one can apply the model equations that have been developed for one flow to the other flow: in this case, from the porous-medium flow to surface-roughness flow.

Turbulent flows over a permeable wall have been considered in many studies [33–39]. The turbulence transport equations in the porous-medium region and homogeneous-fluid region were derived by using both volume- and time-averaging processes [33–36]. Silva and de Lemos [37] numerically investigated the turbulent channel flows with a permeable wall using the turbulence k-ε model with wall function, and DNS was employed in the study by Breugem [38]. Based on the nonlocal form of the volume-averaged momentum equation, the interface condition developed by Ochoa-Tapia and Whitaker [40,41] can be applied at the boundary between a porous-medium and a homogeneous-fluid region as a jump condition in the stress and a continuous-velocity field. The interface jump condition of the turbulent kinetic energy was proposed in the study by de Lemos and Silva [39]. One unique set of transport equations was applied to both regions. The effects of the Reynolds number, porosity, permeability, and jump coefficient on the mean and turbulence fields were investigated.

The Brinkman equation [42] has long been used in studying the averaged flows through complex porous media numerically [43–50] and experimentally [51–54]. The Brinkman equation is a generalized Darcy's law [55] and by neglecting the Forchheimer term at small local Reynolds numbers [38] can be written as

$$\frac{1}{\rho}\langle \nabla P \rangle = -\nu \frac{\varepsilon_\beta}{K} \langle \mathbf{u} \rangle + \nu \nabla^2 \langle \mathbf{u} \rangle \tag{1}$$

where $\mathbf{u}$ is fluid velocity, and $\langle\ \rangle$ denotes the volume average. The equation accounts for the viscous shear effects, the viscous damping effects, and the pressure gradient effects in the low-Reynolds-number region in the porous medium. The solutions of the Brinkman equation represent the averaged flowfield in a partially blocked physical space. The Brinkman equation has been used to facilitate the matching of boundary conditions at the interface between the larger pores and the permeable medium [43–50]. The matching boundary conditions at the interface can be the continuity of the fluid velocity and the pressure between the Brinkman equation and the Navier–Stokes equations solutions.

In light of the geometric and the dynamic similarities between the porous-medium flow and the surface-roughness flow, it is proposed herein to use the Brinkman equation to model the averaged flow in the surface-roughness layer of the turbulent boundary-layer flow, and the outer free-flow region of the turbulent boundary layer will be modeled by the RANS equations. A porous-medium model for surface roughness was initially proposed by Shukla [56] in tribology. Tichy [57] applied the model and treated the rough surface as a porous film in the analysis of the magnetic head flying above the rotating disk in a hard-disk drive.

In this paper, the development of a modeling framework based on such an assumed similarity is described. Boundary-layer types of flows are considered. The flow domain is divided into a rough-wall layer in which the effects of roughness are modeled and an outer free-flow region with fluid only. The fluid dynamics of the averaged flow in the rough-wall layer are resolved by using the Brinkman equation, and the RANS equations are employed in the outer free-flow region. For the Reynolds stress closure, a two-equation k-ε model has been developed. The model incorporates roughness-related closures to an existing smooth-wall low-Reynolds-number model [24] and is employed in both the rough-wall and the free-flow regions. The porosity that appears in the Brinkman equation is determined based on the geometry and the formation of the roughness element. An interface condition [40,41] for the mean velocity and the stresses are

applied at the interface between the rough-wall and the free-flow regions.

In the following sections, the details of the mathematical formulation and the numerical methods used in this study are presented. These are followed by a section in which the simulation results of the new rough-wall-layer modeling using the Brinkman equation are presented.

III. Mathematical Formulation

An incompressible turbulent boundary layer is considered to develop over a surface-roughness region with rigid roughness that is distributed periodically, as shown in Fig. 1. The rough-wall layer, over which the turbulent boundary layer develops, is considered to be thin in comparison with the thickness of the turbulent boundary layer, or $\delta_B \ll \delta$, and undeformable. The local Reynolds number of the flow in roughness region is small. An interface exists between the rough-wall layer and the fluid region.

To incorporate the fact that a typical volume of space can be only partially occupied by fluid in the rough-wall layer, the volume-averaged method [58] is used. The method can be used to derive differential equations for multiphase systems in an averaged sense. The volume-averaged filter provides a spatial smoothing and allows the resulting equations to be valid in the entire domain. As a result of the spatial smoothing, the volume-averaged flow contains negligible variations on the scale smaller than the averaging volume. For the current applications, the detailed flow around the individual roughness element is not resolved. For a fluid property φ associated with the fluid phase β, the intrinsic average can be defined as

$$\langle\varphi\rangle^{\beta} = \frac{1}{\Delta V_{\beta}} \int_{\Delta V_{\beta}} \varphi \mathrm{d}V \tag{2}$$

Similarly, the superficial average can be defined as

$$\langle\varphi\rangle = \frac{1}{\Delta V} \int_{\Delta V} \varphi \mathrm{d}V \tag{3}$$

where ΔV_{β} represents volume occupied by the fluid phase in the averaging volume ΔV. The volume fraction of the fluid phase is generally used as a measure of the porosity ε_{β} of the porous medium defined as

$$\varepsilon_{\beta} = \frac{\Delta V_{\beta}}{\Delta V} \tag{4}$$

The fluid property φ can be defined as the sum of the intrinsic volume average and a deviation φ'':

$$\varphi = \langle\varphi\rangle^{\beta} + \varphi'' \tag{5}$$

The time-averaged value of a fluid property φ associated with the fluid is given as

$$\bar{\varphi} = \lim_{T\to\infty} \frac{1}{T} \int_{t_0}^{t_0+T} \varphi \mathrm{d}t \tag{6}$$

where T is the integration time interval. The instantaneous property can be defined as the sum of the time average and the fluctuating component φ':

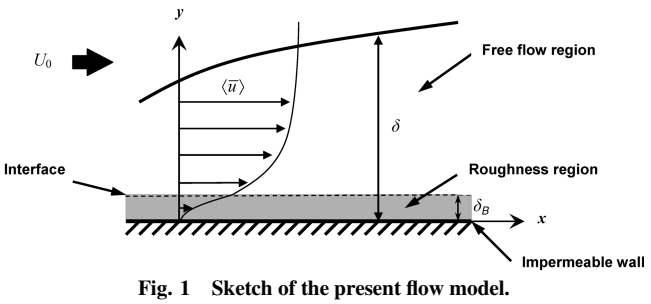

Fig. 1 Sketch of the present flow model.

$$\varphi = \bar{\varphi} + \varphi' \tag{7}$$

It is easy to show that $\langle\bar{\varphi}\rangle = \overline{\langle\varphi\rangle}$, $\langle\varphi'\rangle = \langle\varphi\rangle'$, $\bar{\varphi}'' = \overline{\varphi''}$, and $\varphi''' = \varphi'''$ [36].

The volume-averaged theorem [58] can be used to relate the volume average of a spatial derivative to the spatial derivative of the volume average:

$$\langle\nabla\varphi\rangle = \nabla\langle\varphi\rangle + \frac{1}{\Delta V} \int_{A_i} \mathbf{n}\varphi \mathrm{d}A \tag{8}$$

where A_i represents the interface area and $\mathbf{n}$ is the surface normal vector.

A. Free-Flow Region

In the free-flow region with homogeneous fluid, the dimensionless volume- and time-averaged governing equations for the mean flow can be written in a generalized curvilinear coordinates system ξ^j as follows:

$$J\frac{\partial}{\partial\xi^i}\left(\frac{1}{J}V^i\right) = 0 \tag{9}$$

$$\frac{\partial\langle\bar{u}_i\rangle}{\partial t} + V^j\frac{\partial\langle\bar{u}_i\rangle}{\partial\xi^j} = -\xi^j_{x_i}\frac{\partial\langle\bar{P}\rangle}{\partial\xi^j} + J\frac{\partial}{\partial\xi^j}\left\{\left(\frac{1}{Re}+\nu_t\right)\frac{g^{jp}}{J}\frac{\partial\langle\bar{u}_i\rangle}{\partial\xi^p}\right\} \tag{10}$$

where the Reynolds number Re is defined as U_0L/ν for boundary-layer flows and as U_bH/ν for channel flows, J is the Jacobian of the geometric transformation, and g^{jp} represents the contravariant metric tensor of the geometric transformation defined as

$$g^{jp} = \xi^j_{x_i}\xi^p_{x_i} \tag{11}$$

$$\xi^j_{x_i} = \frac{\partial\xi^j}{\partial x_i} \tag{12}$$

where x_i represents the Cartesian coordinates, and V^j are the contravariant components of the mean Cartesian velocity components $\langle\bar{u}_k\rangle$, defined as

$$V^j = \langle\bar{u}_k\rangle\xi^j_{x_k} \tag{13}$$

The turbulent kinetic energy k and the dissipation rate of the turbulent kinetic energy ε are given as

$$k = \frac{1}{2}\langle\overline{u_i'u_i'}\rangle \tag{14}$$

$$\varepsilon = \frac{1}{Re}\left\langle\overline{\frac{\partial u_i'}{\partial x_j}\frac{\partial u_i'}{\partial x_j}}\right\rangle \tag{15}$$

The transport equations [24] for k and ε are

$$\frac{\partial k}{\partial t} + V^j\frac{\partial k}{\partial\xi^j} = J\frac{\partial}{\partial\xi^j}\left\{\left(\frac{1}{Re}+\frac{\nu_t}{\sigma_k}\right)\frac{g^{jp}}{J}\frac{\partial k}{\partial\xi^p}\right\} + G - \varepsilon - D \tag{16}$$

$$\frac{\partial\varepsilon}{\partial t} + V^j\frac{\partial\varepsilon}{\partial\xi^j} = J\frac{\partial}{\partial\xi^j}\left\{\left(\frac{1}{Re}+\frac{\nu_t}{\sigma_\varepsilon}\right)\frac{g^{jp}}{J}\frac{\partial\varepsilon}{\partial\xi^p}\right\} + C_1f_1\frac{\varepsilon}{k}G - C_2f_2\frac{\varepsilon^2}{k} + E \tag{17}$$

$$\nu_t = C_\mu f_\mu\frac{k^2}{\varepsilon} \tag{18}$$

$$D = \frac{2}{Re}\left(\xi^k_{x_2}\frac{\partial\sqrt{k}}{\partial\xi^k}\right)^2 \tag{19}$$

$$E = \frac{2\nu_t}{Re}\left[\xi^j_{x_2}\frac{\partial}{\partial\xi^j}\left(\xi^k_{x_2}\frac{\partial\langle\bar{u}_2\rangle}{\partial\xi^k}\right)\right]^2 \tag{20}$$

The production term G in Eqs. (16) and (17) can be expressed as follows:

$$G = \frac{1}{2}\nu_t\left(\frac{\partial\langle\bar{u}_i\rangle}{\partial\xi^k}\xi^k_{x_j} + \frac{\partial\langle\bar{u}_j\rangle}{\partial\xi^k}\xi^k_{x_i}\right)^2 \tag{21}$$

The value of the model constants are $\sigma_k = 1.0$, $\sigma_\varepsilon = 1.3$, $C_1 = 1.44$, $C_2 = 1.92$, and $C_\mu = 0.09$.

The damping functions f_μ, f_1, and f_2 proposed by Launder and Sharma [24] are

$$f_\mu = \exp[-3.4/(1 + R_t/50)^2] \tag{22}$$

$$f_1 = 1 \tag{23}$$

$$f_2 = 1 - 0.3\exp(-R_t^2) \tag{24}$$

B. Roughness Region

In the surface-roughness region with thickness δ_B, the analytical solution of the Brinkman equation for a boundary-layer flow with constant porosity can be found [38]:

$$\langle\bar{u}\rangle = (U_I - U_d)\cdot\exp\left[\sqrt{\varepsilon_\beta/Da}\cdot(y-\delta_B)\right] + U_d \tag{25}$$

$$\langle\bar{v}\rangle = \sqrt{Da/\varepsilon_\beta}\cdot\frac{\partial(U_I - U_d)}{\partial x}\cdot\left\{1 - \exp\left[\sqrt{\varepsilon_\beta/Da}\cdot(y-\delta_B)\right]\right\} - \frac{\partial U_d}{\partial x}\cdot(y-\delta_B) - V_I \tag{26}$$

$$U_d = -Re\cdot Da\cdot\frac{d\langle\bar{P}\rangle}{\partial x} \tag{27}$$

where the Darcy number Da is defined as K/L^2 for boundary-layer flows and as K/H^2 for channel flows (therefore, in the roughness region, the streamwise flow component decays exponentially toward the impermeable lower wall), and U_I and V_I are the slip velocity components in the streamwise and the wall-normal directions, respectively. The slip velocity at the interface will be determined by coupling with the free-flow region solutions via the interface conditions that will be discussed later.

The dimensionless volume- and time-averaged governing equations for the disturbances in the roughness region with constant porosity and permeability can be written in a generalized curvilinear coordinates system ξ^j [24,33–37]. The model equations are

$$\frac{\partial k}{\partial t} + \frac{1}{\varepsilon_\beta}V^j\frac{\partial k}{\partial\xi^j} = J\frac{\partial}{\partial\xi^j}\left\{\left(\frac{1}{Re} + \frac{\nu_{t_\beta}}{\sigma_k}\right)\frac{g^{jp}}{J}\frac{\partial k}{\partial\xi^p}\right\} + \frac{1}{\varepsilon_\beta}G - \varepsilon - D - F_i\langle\bar{u}_i\rangle \tag{28}$$

$$\frac{\partial\varepsilon}{\partial t} + \frac{1}{\varepsilon_\beta}V^j\frac{\partial\varepsilon}{\partial\xi^j} = J\frac{\partial}{\partial\xi^j}\left\{\left(\frac{1}{Re} + \frac{\nu_{t_\beta}}{\sigma_\varepsilon}\right)\frac{g^{jp}}{J}\frac{\partial\varepsilon}{\partial\xi^p}\right\} + C_1 f_1\frac{\varepsilon}{k}\frac{1}{\varepsilon_\beta}G - C_2 f_2\frac{\varepsilon^2}{k} - E - C_3\frac{\varepsilon}{k}F_i\langle\bar{u}_i\rangle \tag{29}$$

$$F_i = -\frac{1}{Re\cdot Da}\langle\bar{u}_i\rangle \tag{30}$$

$$\nu_{t_\beta} = \frac{\nu_t}{\varepsilon_\beta} \tag{31}$$

It should be noted that applying the time- and volume-averaged operators in different sequences can lead to different turbulence governing equations [33–37]. Defining the turbulent kinetic energy in a porous-medium flow is still an open question. Pedras and de Lemos [59] showed that the turbulent kinetic energy obtained by applying the time-averaged operator on top of the volume-averaged operator does not account for all of the turbulent kinetic energy associated with flow. Although there are differences in the turbulence governing equations obtained by using the two different approaches, the same final closure models for these equations can be reached when considering their respective turbulent kinetic energies (i.e., $k = \frac{1}{2}\langle u_i' u_i'\rangle$ and $k = \frac{1}{2}\overline{\langle u_i\rangle'\langle u_i\rangle'}$ [35,36]). In the present model, the model equation for the turbulent kinetic energy k and its dissipation rate ε are Eqs. (28) and (29), with k and ε defined in Eqs. (14) and (15), respectively. Except for the drag-force F_i-related terms, the model equations are the same as those used in the free-flow region. The drag force F_i has its origin in the volume-averaged Navier–Stokes equations [60]. As has been frequently invoked in porous-medium studies, the Forchheimer correction tenor [60] is assumed to be negligible, because the local Reynolds number of the flow in the roughness region is considered to be small [38]. The last term on the right-hand side of Eq. (28) represents the work done by the drag force. The drag-force term in Eq. (29) has been obtained by a simple scaling of the corresponding term in Eq. (28). As a result, the coefficient C_3 is a model constant; it was set at 0.11.

For the permeability K, a widely used correlation [58] in porous-medium flow studies is employed. The resulting Darcy number Da can be written as

$$Da = \frac{\varepsilon_\beta^3 d_p^2}{180(1-\varepsilon_\beta)^2} \tag{32}$$

C. Interface Region

For the flow involving a wall roughness and an unobstructed free-flow region, an interface is identified between the free-flow and the roughness regions. The interface conditions developed by Ochoa-Tapia and Whitaker [40,41] assumed a jump relation for the intrinsic stresses and a continuous superficial velocity across the interface. In this study, the interface conditions [37,38,40,41] are adopted for the averaged flow properties, and the turbulence model quantities k and ε are assumed to be continuous [37]:

$$\langle\bar{u}\rangle|_{\text{roughness}} = \langle\bar{u}\rangle|_{\text{free flow}} = U_I \tag{33}$$

$$\left(\frac{1}{\varepsilon_\beta\cdot Re} + \nu_{t_\beta}\right)\frac{\partial\langle\bar{u}\rangle}{\partial y}\bigg|_{\text{roughness}} - \left(\frac{1}{Re} + \nu_t\right)\frac{\partial\langle\bar{u}\rangle}{\partial y}\bigg|_{\text{free flow}} = \left(\frac{1}{Re} + \nu_t\right)\frac{\beta_t}{\sqrt{Da}}U_I \tag{34}$$

$$\langle\bar{v}\rangle|_{\text{roughness}} = \langle\bar{v}\rangle|_{\text{free flow}} = V_I \tag{35}$$

$$\left(\frac{1}{\varepsilon_\beta \cdot Re} + \nu_{t_\beta}\right)\frac{\partial\langle\bar{v}\rangle}{\partial y}\bigg|_{\text{roughness}} - \left(\frac{1}{Re} + \nu_t\right)\frac{\partial\langle\bar{v}\rangle}{\partial y}\bigg|_{\text{free flow}} = \left(\frac{1}{Re} + \nu_t\right)\frac{\beta_n}{2\sqrt{Da}}V_I \tag{36}$$

$$1/\varepsilon_\beta\langle\bar{P}\rangle|_{\text{roughness}} = \langle\bar{P}\rangle|_{\text{free flow}} \tag{37}$$

$$k|_{\text{roughness}} = k|_{\text{free flow}} \tag{38}$$

$$\varepsilon|_{\text{roughness}} = \varepsilon|_{\text{free flow}} \tag{39}$$

where β_t and β_n are the tangential and normal stress jump parameters, respectively. The value of stress jump parameters might be chosen to accommodate engineering flows over porous media. The results of de Lemos and Silva [39] showed that a negative tangential stress jump parameter gave results that agreed with the experimental data for the turbulent kinetic energy at the interface. In this study, we use $\beta_t = -1$ and $\beta_n = 5$. The constants were set based on generally accepted values. They have not been selected or optimized for the calculation results shown here.

To form a closure model, the effective diameter parameter d_P and the thickness of the roughness region δ_B need to be provided. We propose to relate d_P with the height of physical roughness k_s. This provides a direct link between the physical length scale and that needed for the modeling. The proposed expression satisfies the length-scale constraint that d_P is small compared with k_s [58] and has the following form:

$$d_p = (1 - \varepsilon_\beta)^3\varepsilon_\beta^2 k_s \tag{40}$$

Similarly, the thickness, or the height, of the roughness region δ_B, in which the effects of the surface roughness are modeled, should also be related to the height of the actual roughness. In this work, the following form is used:

$$\delta_B = (1 - \varepsilon_\beta)\varepsilon_\beta k_s \tag{41}$$

For all of the cases presented in this paper, the correlation gives the heights of the modeled roughness regions that are lower than those of the log-law layers. This conforms with the use of the Brinkman equation in the modeled roughness region in the present modeling framework.

In summary, in the current k-ε formulation of the Brinkman equation modeling approach, the model equations are developed based on an existing smooth-wall turbulence model, and roughness-related model parameters are introduced. The parameters are C_3 in Eq. (29), d_P in Eq. (40), and δ_B in Eq. (41). For the present model, the flow domain is divided into a roughness region in which the effects of roughness are modeled and a free-flow region with fluid only, as shown in Fig. 1. The fluid dynamics of the averaged flow in the roughness region are determined using Eqs. (25) and (26), and the turbulent quantities needed for closure are resolved using Eqs. (28) and (29). The mean flow and turbulent characteristics in the free-flow region are resolved using Eqs. (9) and (10) and Eqs. (16) and (17), respectively. The interface conditions [Eqs. (33–39)] enforced the continuity of velocity, pressure, and turbulence properties and the stress jump condition at the interface between the roughness and the free-flow regions. The interface slip velocities thus obtained are then used to determine the averaged flow [Eqs. (25) and (26)] in the roughness region for next iteration.

IV. Numerical Methods

The numerical method employed in the study by Lu and Liou [61] has been used to solve the dimensionless RANS equations in the generalized curvilinear coordinates. The governing equations are discretized spatially on a nonstaggered grid by using second-order approximations (e.g., second-order-accurate upwind differencing for the convective terms and second-order-accurate central finite differencing for the viscous terms). Temporally, a four-stage explicit Runge–Kutta scheme is used. This numerical methodology has been tested and validated for a wide range of laminar flows and turbulent flows with various turbulence closures [61–64].

The mean flow and the turbulence modeling equations are solved in a weakly coupled manner. The Courant–Friedrichs–Lewy number used in these computations is 1.5 for both the k and ε equations. The numerical solution process was regarded as converged with a four- to five-order-of-magnitude decrease of residuals.

A. Computational Domains

In this study, two-dimensional solutions for channel and flat-plate flows are sought. The computational domain corresponding to the fully developed turbulent smooth and rough channel flows extends 150 channel heights downstream. The flows are assumed to be symmetric along the centerline. For the turbulent boundary layers over smooth and rough plates, the computational domain extends one plate length downstream. For all of the cases calculated, the resulting thicknesses of the modeled roughness region δ_B are below the log-law region ($\delta_B^+ < 30$).

B. Boundary Conditions

The boundary conditions were specified as follows. The inlet boundary conditions for the fully developed turbulent smooth channel flows are assumed uniform for all variables, in which $\langle\bar{u}\rangle = 1$, $\langle\bar{v}\rangle = 0$, and $k = \varepsilon = 10^{-6}$. For the smooth flat plates, the Blasius solution has been used at the inlet with uniform profiles of $k = 0.013$ and $\varepsilon = 7$ [61]. The smooth-wall solutions thus obtained are then used to initialize the corresponding rough-wall calculations. As for the symmetry boundaries, the mirror-image reflections for the grid and the flow variables are used for the fully developed turbulent smooth and rough channel flows. For all cases, the exit boundary condition is imposed by assuming zero streamwise diffusion. At the outer boundary of the flat plate, the turbulent boundary layer assumes the corresponding freestream conditions. The wall boundary condition is a zero value for all variables: that is, $\langle\bar{u}\rangle = \langle\bar{v}\rangle = k = \varepsilon = 0$.

C. Grid-Independent Study

For the channel flows, the numerical grid in the wall-normal direction is generated by using a hyperbolic stretching function. The grid clusters near the inlet and is stretched using a hyperbolic stretching function toward the exit in the streamwise direction. A grid-independent study for smooth channel flow has been performed, and the results are shown in Fig. 2. Figure 2 also shows the calculated log-law velocity profiles by using the present rough-wall-layer modeling with zero roughness-region thickness ($\delta_B = 0$) on grids of 91×141, 55×141, 91×181, and 55×181 in the streamwise and

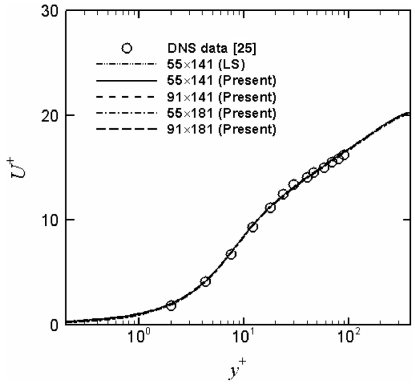

Fig. 2 Grid-independent study with grid refinement in the wall-normal direction.

the wall-normal directions, respectively. The Reynolds number, based on the channel height, is 13,750. The DNS data [25] are also included for comparison. Note that for a smooth wall, the present model naturally reduces to the baseline model of Launder and Sharma (LS) [24]. The computed profiles using the different grids collapse, indicating that the turbulent flow solutions are grid-independent. The 55×141 grid is used in all of the channel-flow solutions presented here. For the flat-plate boundary flows, a hyperbolic tangent stretching function has been used in the wall-normal direction with a grid clustered in the near-wall region. The value of y^+ for the first grid point away from the wall is less than 0.1. The grid clusters near the inlet and is stretched using a hyperbolic stretching function toward the exit in the streamwise direction. Figure 3 shows the surface skin-friction distributions, which are known to be sensitive to numerical grids, and Fig. 4 shows the computed mean velocity profiles. The grid sizes vary between 71×150 and 281×150 (Fig. 3) and between 141×150 and 141×180 (Fig. 4). The results show that the numerical code achieves grid-independent solutions for the flat-plate turbulent boundary layer. The turbulent flat-plate boundary-layer flow results presented have been obtained by using the 141×150 grid.

V. Results and Discussion

The results are reported and discussed in three sections. Section V.A presents the calculation results of the present model with zero roughness-region thickness ($\delta_B = 0$) in fully developed turbulent smooth channel flows and smooth-wall turbulent boundary layers and their comparisons with the corresponding DNS data and experimental measurements. Results for fully developed rough channel flows and turbulent boundary layers over different types of surface roughness are presented in Secs. V.B and V.C. The results shown include the skin-friction coefficient, the roughness function variation, the mean velocity, and turbulent quantity profiles. When appropriate, the results are also compared with previous solutions [61] obtained by using the model of Foti and Scandura [23].

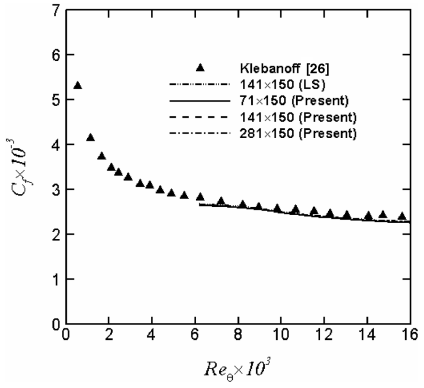

Fig. 3 Grid-independent study for flat plates with grid refinement in the streamwise direction.

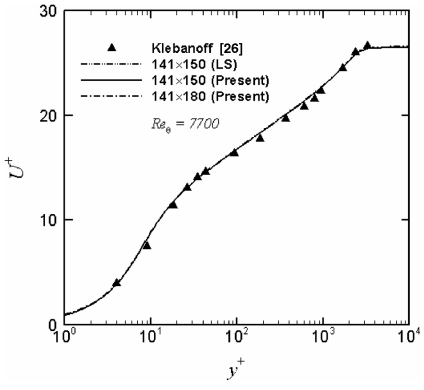

Fig. 4 Grid-independent study for flat plates.

A. Smooth Channel Flows and Smooth-Wall Turbulent Boundary Layers

For the fully developed turbulent smooth channel flows, the computational results are compared with the DNS data [25] at a Reynolds number, based on the channel height, of 13,750. As was mentioned earlier, in this case, the present low-Reynolds-number k-ε model naturally reduces to that of the LS model. The comparisons of the log-law velocity and the turbulent kinetic energy are shown in Figs. 2 and 5, respectively. It is shown in Fig. 2 that the predicted log-law velocity profile collapses with that of the LS model and agrees well with the data. The calculated turbulent kinetic energy agrees well with that from the LS model.

The turbulent boundary-layer flow over a smooth plate is also calculated. The experimental results of Klebanoff [26] for $Re_\theta = 7700$ are used here for comparison. Figure 3 shows that the calculated skin-friction coefficients are in a good agreement with the experimental data. The computed log-law velocity profiles shown in Fig. 4 also agree well with the data in the sublayer and outer layer. The results of the turbulent kinetic energy and the Reynolds shear stress across the boundary layer are shown in Fig. 6. The present results agree well with those obtained by using the LS model.

B. Rough Channel Flows

The fully developed rough channel flows of Bakken et al. [27] are calculated. Two different rough surfaces (Fig. 7) [i.e., mesh roughness of $k_s^+ = 83$ ($k_{\text{eq}}^+ = 273.9$) and square-rod roughness of $k_s^+ = 107$ ($k_{\text{eq}}^+ = 834.6$)] were examined. The Reynolds numbers, based on the channel height, are 62,000 and 60,000 for the mesh and the square-rod roughness, respectively. The porosity is calculated based on the volumetric characteristics of the roughness. The total stress method is used to determine the friction velocity u_τ. This method assumes that a constant-stress region exists in the inner layer of the boundary layer; that is,

$$u_\tau = \left[\frac{1}{Re}\frac{\partial\langle\bar{u}\rangle}{\partial y} - \langle\overline{u'v'}\rangle\right]^{1/2} \tag{42}$$

where $\langle\overline{u'v'}\rangle$ represents superficial average Reynolds shear stress.

The calculated distribution of the log-law velocity, the Reynolds shear stress, and the turbulent kinetic energy across the channel are shown.

1. *Mesh Roughness*

For the type of mesh roughness [27] shown in Fig. 7a, the porosity can be readily calculated with a given square-pattern center spacing λ and width b:

$$\varepsilon_\beta = \frac{\Delta V_\beta}{\Delta V} = \frac{(\lambda - b)\cdot(\lambda - b)\cdot k_s}{\lambda \cdot \lambda \cdot k_s} = \left[1 - \frac{b}{\lambda}\right]^2 \tag{43}$$

For Bakken et al. [27], $k_s = 0.015H$, $\lambda = 0.12H$, and $b = 0.02H$. The resulting porosity and Darcy number are 0.694 and

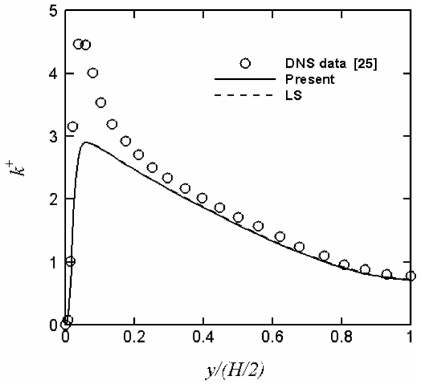

Fig. 5 Comparisons of the turbulent kinetic energy in smooth channel flows.

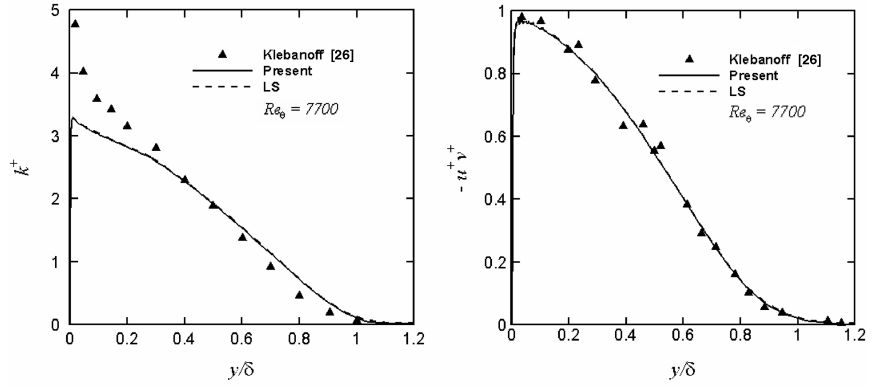

Fig. 6 Comparisons for a smooth-wall turbulent boundary layer: a) turbulent kinetic energy and b) Reynolds shear stress.

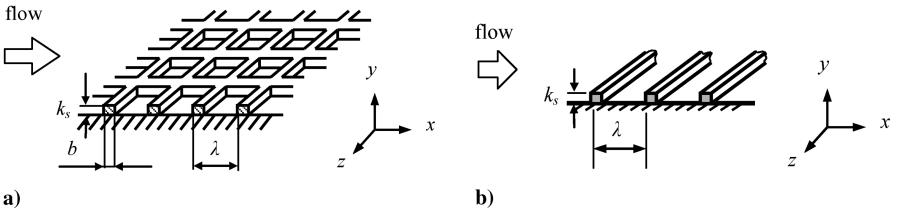

Fig. 7 Sketch of surface roughness: a) mesh and b) square rod.

8.498×10^{-10}, respectively. The computed log-law velocity and the Reynolds shear stress, comparing with the numerical predictions from Foti and Scandura (FS) [23] and the measurements are shown in Figs. 8 and 9, respectively. Figure 8 shows that the present model well predicts the log-law velocity profile. The FS model predicts the correct slope, but underpredicts the roughness function ΔU^+. Figure 9 shows that the calculated Reynolds shear stress profiles from both models agree with the experimental data in the outer region of $y/(H/2) > 0.2$. In the inner region of $y/(H/2) < 0.2$, the peak level of the measured Reynolds shear stress profile is lower than the predictions. The reduced-peak Reynolds shear stress has been attributed to the local flow acceleration ahead of and above the mesh roughness [27]. In the current calculations, the roughness function ΔU^+ is determined by

$$\Delta U^+ = \left(\sqrt{2/C_f}\right)_{\text{smooth}} - \left(\sqrt{2/C_f}\right)_{\text{rough}} \tag{44}$$

and the skin-friction coefficient from the present model is calculated using the following expression in the constant total stress layer:

$$C_f = 2\left[\frac{1}{Re}\frac{\partial\langle\bar{u}\rangle}{\partial y} - \langle\overline{u'v'}\rangle\right] \tag{45}$$

2. Square-Rod Roughness

For the square-rod roughness [27] shown in Fig. 7b, the porosity can be readily calculated with a given center-to-center spacing λ:

$$\varepsilon_\beta = \frac{\Delta V_\beta}{\Delta V} = \frac{(\lambda \cdot k_s - k_s \cdot k_s)}{\lambda \cdot k_s} = 1 - \frac{k_s}{\lambda} \tag{46}$$

where $k_s = 0.017H$ and $\lambda = 0.136H$ for Bakken et al. [27]. The resulting porosity and Darcy number are 0.875 and 1.539×10^{-10}, respectively. Figure 10 shows the calculated log-law velocity profiles. It can be observed that the log-law velocity profile predicted by the present model agrees well with the experimental data. The FS model predicts the correct slope, yet it underpredicts the roughness function ΔU^+. The computational results of the Reynolds shear stress and the turbulent kinetic energy, comparing with the numerical predictions from the FS model and the measurements, are shown in Figs. 11 and 12, respectively. The Reynolds shear stress profile calculated by using the FS model agrees better with the data than that from the present model for the outer region of $y/(H/2) > 0.2$. Both models underpredict the turbulent kinetic energy as reported by the experimental data (Fig. 12).

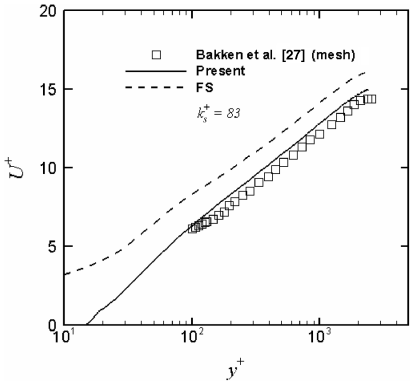

Fig. 8 Comparisons of the log-law velocity in rough channel flows with mesh roughness.

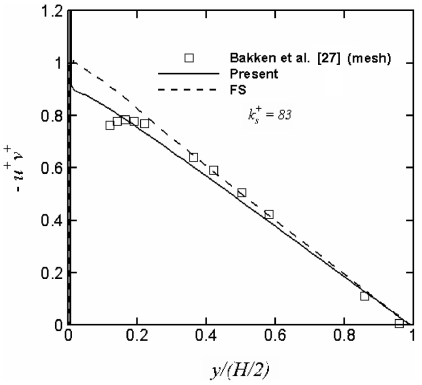

Fig. 9 Comparisons of the Reynolds shear stress in rough channel flows with mesh roughness.

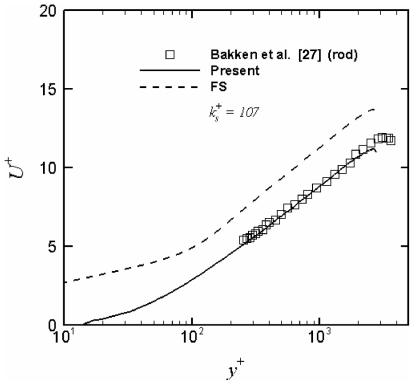

Fig. 10 Comparisons of the log-law velocity in rough channel flows with square-rod roughness.

C. Turbulent Boundary Layers over Rough Plates

The turbulent boundary layers over a flat plate with different types of surface roughness were calculated. They include woven mesh [28,29], cylinder [30], square rod [31], and perforated plate [32]. The roughness Reynolds number k_s^+ ranges between 94.6 and 150. Based on the geometry of the roughness elements and their formations provided by the corresponding experimental measurements, the porosity ε_β for these different types of surface roughness vary from 0.398 to 0.898. Comparisons of the log-law velocity, the Reynolds shear stress, and the turbulent kinetic energy across the turbulent boundary layers are shown.

1. *Mesh Roughness*

For the mesh roughness [28] of $k_s = 1.38$ mm and $k_s^+ = 94.6$ ($k_{\text{eq}}^+ = 340$) shown in Fig. 13, the porosity is calculated with the given square-pattern center spacing λ and wire diameter d_w using the following formulation:

$$\varepsilon_\beta = \frac{\Delta V_\beta}{\Delta V} = \frac{[\lambda \cdot \lambda \cdot k_s - 2(\pi \cdot d_w^2/4 \cdot \lambda)]}{\lambda \cdot \lambda \cdot k_s} = 1 - \frac{\pi \cdot d_w^2/2}{\lambda \cdot k_s} \quad (47)$$

where $\lambda = 3.18$ mm and $d_w = 0.69$ mm for Antonia and Krogstad [28]. The resulting porosity $\varepsilon_\beta = 0.83$ and $Da = 6.30 \times 10^{-13}$. The experiment study was conducted at a Reynolds number, based on the plate length, of 4.62×10^6, and the data were measured at $Re_\theta = 12,800$.

A comparison of the calculated log-law velocity with that by using the FS model and the experimental measurements is provided in Fig. 14. It is shown that the results of the present model agree satisfactorily with the experimental data in the log law and the outer-layer regions. The difference in the skin-friction coefficient between the present calculations and the measurements is about 4.5%, compared with about 15% for that by the FS model. The computed Reynolds shear stress and turbulent kinetic energy are shown in Figs. 15 and 16, respectively. The Reynolds shear stress profiles calculated by both models agree with the experimental data and broadly follow the trend of the experimental data, as shown in Fig. 15a. The present model employed an interface condition [40,41] that characterizes the slip velocity at the top of the modeled roughness region by a jump of the velocity gradient across the interface. This results in a discontinuity of the Reynolds shear stress at the interface. Figure 15b shows a close-up of the Reynolds shear stress distribution in the near-wall roughness region. The modeled interface is located at $y/\delta = 0.004$, and the calculated streamwise slip velocity is $U^+ = 0.48$. Except for nearing the interface, the present model describes a much-reduced turbulent momentum transport in the modeled roughness layer, compared with that using the FS model, which essentially maintains the same level of the Reynolds stress in the roughness region. Turbulent fluctuations are mostly dampened in the roughness region. It is reasonable to expect that this damping effect, as is reflected in the present model results, lessens near the interface in which the flow motion is far less restricted. It is shown in Fig. 16 that both models less satisfactorily predict the turbulent kinetic energy across the boundary layer.

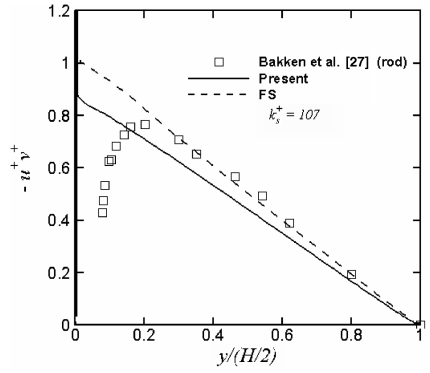

Fig. 11 Comparisons of the Reynolds shear stress in rough channel flows with square-rod roughness.

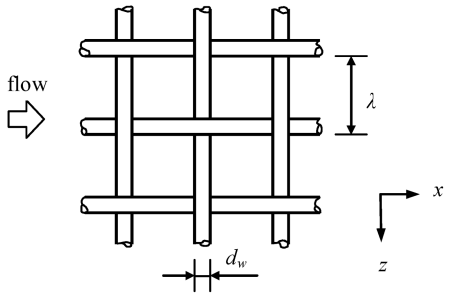

Fig. 13 Sketch of woven-mesh roughness.

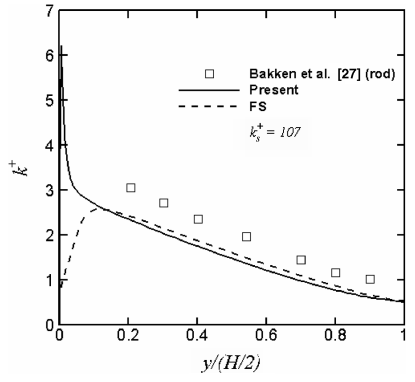

Fig. 12 Comparisons of the turbulent kinetic energy in rough channel flows with square-rod roughness.

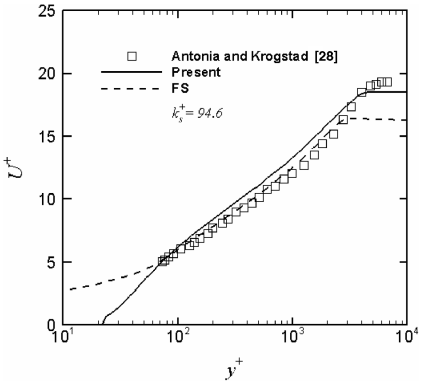

Fig. 14 Comparisons of the log-law velocity at $Re_\theta = 12,800$ in turbulent boundary layer with woven-mesh roughness.

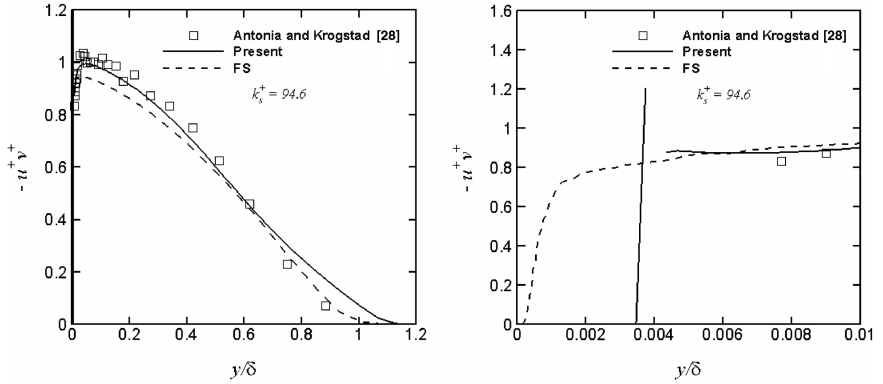

Fig. 15 Comparisons of the Reynolds shear stress at $Re_\theta = 12,800$ in turbulent boundary layer with woven-mesh roughness.

2. Woven-Mesh Roughness

For the woven-mesh roughness [29] of $k_s = 1.40$ mm and $k_s^+ = 150$ ($k_{\text{eq}}^+ = 370$), similar to that shown in Fig. 13, the porosity is calculated using Eq. (47) with $\lambda/d_w = 4.58$ [29]. The resulting porosity $\varepsilon_\beta = 0.829$ and $Da = 8.943 \times 10^{-13}$. The experimental study by Flack et al. [29] was conducted at a Reynolds number, based on the plate length, of 2.7×10^6, and the data were measured at $Re_\theta = 9110$. The computed mean velocity and the Reynolds shear stress are shown in Figs. 17 and 18, respectively. It can be observed that the mean velocity profiles predicted by both models agree well with the experimental data in the log-law region. The present model provides the better prediction in the outer region than that of the FS model. The simulation results of both models show that the Reynolds shear stress profiles generally follow the trend of the experimental data and are in good agreement with the data across the turbulent boundary layer.

3. Cylinder Roughness

For the cylinder roughness [30] of $k_s = 1.52$ mm and $k_s^+ = 128$ shown in Fig. 19, the porosity can be calculated using square-pattern center spacing λ and cylinder diameter d_c as

$$\varepsilon_\beta = \frac{\Delta V_\beta}{\Delta V} = \frac{[\lambda \cdot \lambda \cdot k_s - \pi \cdot d_c^2/4 \cdot k_s]}{\lambda \cdot \lambda \cdot k_s} = 1 - \frac{\pi \cdot d_c^2/4}{\lambda^2} \tag{48}$$

For $\lambda = 5.486$ mm and $d_c = 1.98$ mm [30], the resulting porosity $\varepsilon_\beta = 0.898$ and $Da = 7.853 \times 10^{-14}$. The experimental study by George and Simpson [30] was conducted at a Reynolds number, based on the plate length, of 4.82×10^6, and the data were measured at the half-spacing λ location directly behind the cylinder. The FS model was not carried out for comparison, because the equivalent sand roughness k_{eq}^+, which is a FS model parameter, was not provided by George and Simpson.

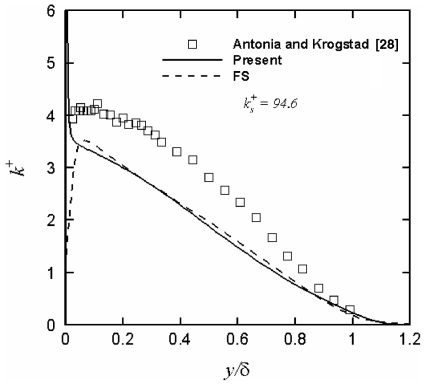

Fig. 16 Comparisons of the turbulent kinetic energy at $Re_\theta = 12,800$ in turbulent boundary layer with woven-mesh roughness.

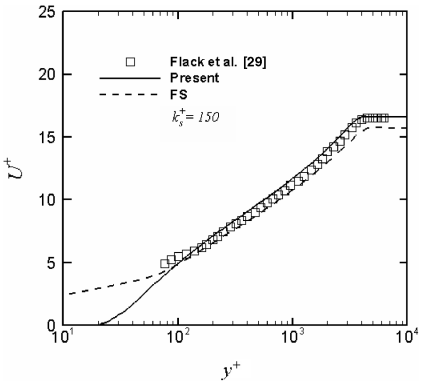

Fig. 17 Comparisons of the log-law velocity at $Re_\theta = 9110$ in turbulent boundary layer with surface roughness of mesh.

It is shown in Fig. 20 that the simulation results of the present model agree with the experimental data in the log-law region at $Re_\theta = 13,789$. The calculated freestream U^+ is slightly lower than the measurement. As the data were taken directly behind a cylinder

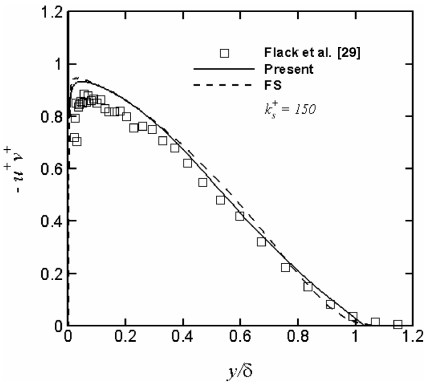

Fig. 18 Comparisons of the Reynolds shear stress at $Re_\theta = 9110$ in turbulent boundary layer with surface roughness of mesh.

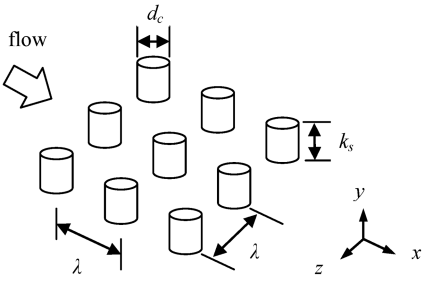

Fig. 19 Sketch of cylinder roughness.

roughness, a small reverse-flow region is measured. The computed Reynolds shear stress and the turbulent kinetic energy are shown in Figs. 21 and 22, respectively. It can be observed from Fig. 21 that the predicted Reynolds shear stress profile agrees well with the experimental data in the region in which $y/\delta > 0.1$. For the turbulent kinetic energy (Fig. 22), the calculated distribution is less satisfactory. The measured Reynolds shear stress and turbulent kinetic energy profiles show enhanced peaks near the top of the cylinder roughness.

Arguably, the shear-production mechanism associated with the flow around a roughness element is generally captured in the present modeling approach in an (volume) average manner.

4. Square-Rod Roughness

For the square-rod roughness [31] of $k_s = 3$ mm and $k_s^+ = 150$, similar to that shown in Fig. 7b, the porosity is calculated using Eq. (46) with $\lambda = 10$ mm [31]. The resulting porosity $\varepsilon_\beta = 0.7$ and $Da = 1.334 \times 10^{-12}$. The experimental study by Keirsbulck et al. [31] was conducted at a Reynolds number, based on the plate length, of 3.94×10^6, and the data were measured at $Re_\theta = 8549$. The FS model was not carried out for comparison, because the required equivalent sand roughness k_{eq}^+ was not provided by Keirsbulck et al. [31]. The computed mean velocity and the Reynolds shear stress are shown in Figs. 23 and 24, respectively. The mean velocity profile predicted by the present model agrees well with the experimental data in the log-law layer region and in the outer-layer region. The predicted Reynolds shear stress profile from the present model is in a good agreement with the experimental data for the region of $y/\delta > 0.6$. The measured peak Reynolds shear stress level is lower than that calculated and decreases at a faster rate toward the wall than reported for other types of roughness in boundary layers [28–30].

5. Perforated-Plate Roughness

For the perforated-plate roughness [32] of $k_s = 0.9$ mm and $k_s^+ = 122$ ($k_{eq}^+ = 149$) as shown in Fig. 25, the porosity can be calculated

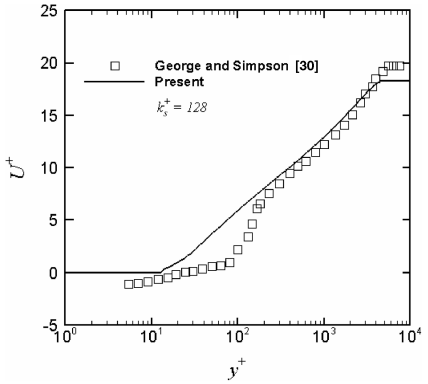

Fig. 20 Comparisons of the log-law velocity at $Re_\theta = 13,789$ in turbulent boundary layer with surface roughness of circular cylinders.

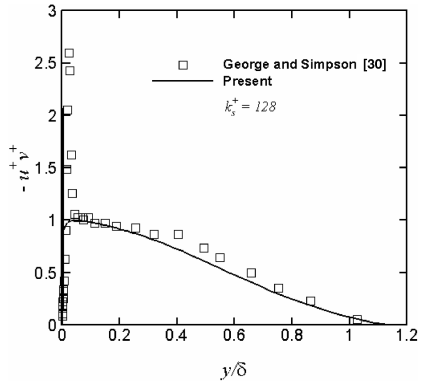

Fig. 21 Comparisons of the Reynolds shear stress at $Re_\theta = 13,789$ in turbulent boundary layer with surface roughness of circular cylinders.

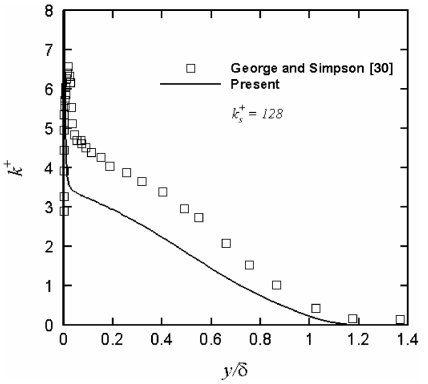

Fig. 22 Comparisons of the turbulent kinetic energy at $Re_\theta = 13,789$ in turbulent boundary layer with surface roughness of circular cylinders.

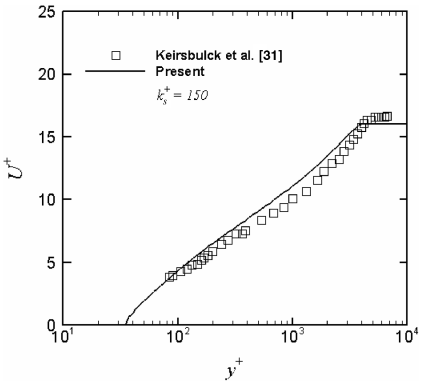

Fig. 23 Comparisons of the log-law velocity at $Re_\theta = 8549$ in turbulent boundary layer with surface roughness of square rods.

using the square-pattern center spacing λ and the circular hole diameter d_h as

$$\varepsilon_\beta = \frac{\Delta V_\beta}{\Delta V} = \frac{\pi \cdot d_h^2/4 \cdot k_s}{\lambda \cdot \lambda \cdot k_s} = \frac{\pi \cdot d_h^2/4}{\lambda^2} \tag{49}$$

where $\lambda = 2.81$ mm and $d_h = 2$ mm [32]. The resulting porosity $\varepsilon_\beta = 0.398$ and $Da = 3.3487 \times 10^{-13}$. The experiment was conducted at a Reynolds number, based on the plate length, of 4.44×10^6, and is among the few available experimental measurements that provide the streamwise variation of skin-friction coefficient. For the experimental study [32], the skin-friction coefficient is calculated using Eq. (45), which is also used in the present model to determine the skin-friction coefficient. The skin-friction coefficient for the FS model is determined directly from the wall shear stress. The computed streamwise development of the skin-friction coefficients are presented in Fig. 26. The present model well

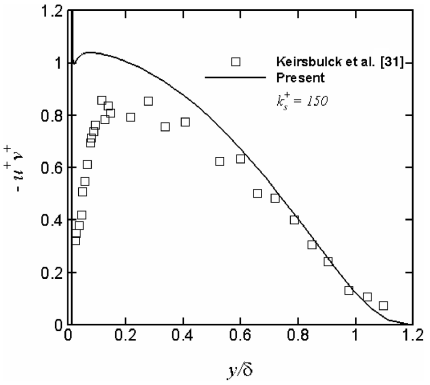

Fig. 24 Comparisons of the Reynolds shear stress at $Re_\theta = 8549$ in turbulent boundary layer with surface roughness of square rods.

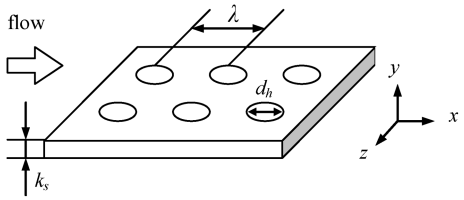

Fig. 25 Sketch of a perforated plate.

predicts the skin-friction coefficient changes in the streamwise direction. For example, the differences between the predictions and measurements are about 4% for the present model at $Re_\theta = 11,460$ and about 19% for the FS model. The profiles of the log-law velocity at $Re_\theta = 11,460$ are compared in Fig. 27. It is shown that the predictions from the present model agree well with the experimental data in the log-law and the outer-layer regions. The predicted profile from the FS model collapses to the experimental data in the log layer but diverges from the data in the outer layer.

In the preceding, the present model results for seven different rough-wall cases have been shown. The results were compared individually with those reported in the corresponding experimental studies. To provide an overall comparison, the calculated roughness functions for all of these different cases are plotted in Fig. 28 versus their equivalent sand roughness k_{eq}^+ and are compared with Prandtl and Schlichting [65]. The roughness functions predicted by the present model agree well with Prandtl and Schlichting over the entire range of k_{eq}^+ calculated. In addition, in the region in which the k_{eq}^+ for the rough channel flows overlaps with that for the rough boundary layers, the predictions consistently agree with Prandtl and Schlichting. This is an encouraging observation for the present modeling approach as, unlike the FS model, k_{eq}^+ is not a model parameter in the present model formulation. It indicates that the present modeling approach that explicitly accounts for the geometry

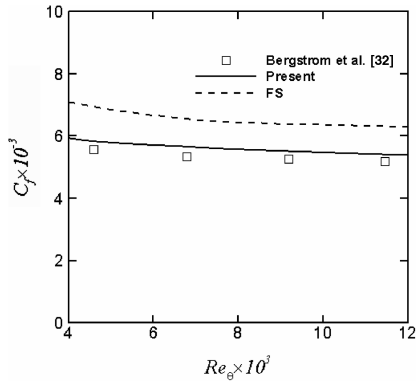

Fig. 26 Predictions of the skin-friction coefficients in turbulent boundary layer with surface roughness of a perforated plate.

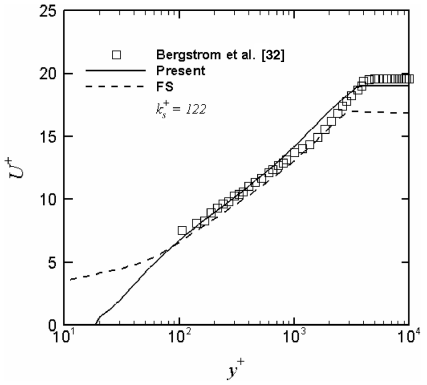

Fig. 27 Comparisons of the log-law velocity at $Re_\theta = 11,460$ in turbulent boundary layer with surface roughness of a perforated plate.

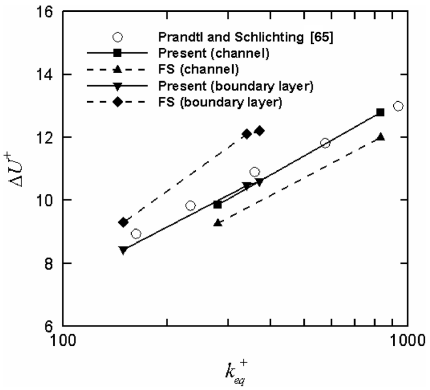

Fig. 28 Comparisons of the roughness functions in terms of equivalent sand roughness heights.

and the formation of the roughness element can lead to more consistent and reliable predictions of the mean flow.

VI. Conclusions

A new flow-physics-based surface-roughness model is developed for the Reynolds-averaged Navier–Stokes-equations numerical calculations of the high-Reynolds-number turbulent flows over rough walls. Based on the results reported, we can conclude that the present model well predicts the skin-friction coefficient, the log-law mean velocity, and the roughness function for the calculated fully developed turbulent rough channel flows and the rough-wall turbulent boundary layers over different types of surface roughness. The proposed roughness modeling approach explicitly takes into account the effect of the formation and the topographical characteristics of the roughness and resolves the fluid dynamics of the averaged flow in the roughness region using the Brinkman equation. The results show that for the case presented, the new physics-based modeling approach can lead to a consistent and reliable modeling of the mean flow for a wide range of roughness types. A two-equation formulation has been adopted for turbulence modeling in the current implementation. In principle, other forms of turbulence closure modeling (for example, second-order Reynolds stress models) can also be adopted to the proposed rough-wall-layer modeling framework.

Acknowledgment

This work has been financially supported by the Office of Naval Research and is gratefully acknowledged.

References

[1] Patel, V. C., "Perspective: Flow at High Reynolds Number and over Rough Surface—Achilles Heel of CFD," *Journal of Fluids Engineering*, Vol. 120, No. 3, 1998, pp. 434–444. doi:10.1115/1.2820682

[2] Miyake, Y., Tsujimoto, K., and Agata, Y., "DNS of a Turbulent Flow in a Rough-Wall Channel Using Roughness Elements Model," *JSME International Journal, Series B (Fluids and Thermal Engineering)*, Vol. 43, No. 2, 2000, pp. 233–242.

[3] Miyake, Y., Tsujimoto, K., and Nakaji, M., "Direct Numerical Simulation of Rough-Wall Heat Transfer in a Turbulent Channel Flow," *International Journal of Heat and Fluid Flow*, Vol. 22, No. 3, 2001, pp. 237–244. doi:10.1016/S0142-727X(01)00085-6

[4] Li, A., and Shao, Y., "Numerical Simulation of Drag Partition over Rough Surfaces," *Boundary-Layer Meteorology*, Vol. 108, No. 3, 2003, pp. 317–342. doi:10.1023/A:1024179025508

[5] Scotti, A., "Direct Numerical Simulation of Turbulent Channel Flows with Boundary Roughened with Virtual Sandpaper," *Physics of Fluids*, Vol. 18, No. 3, 2006, p. 031701. doi:10.1063/1.2183806

[6] Goldstein, D., Handler, R., and Sirovich, L., "Direct Numerical Simulation of Turbulent Flow over a Modelled Riblet Covered

Surface," *Journal of Fluid Mechanics*, Vol. 302, No. 10, 1995, pp. 333–376.
doi:10.1017/S0022112095004125

[7] Lee, C., "Large-Eddy Simulation of Rough-Wall Turbulent Boundary Layers," *AIAA Journal*, Vol. 40, No. 10, 2002, pp. 2127–2130.
doi:10.2514/2.1548

[8] Cui, J., Patel, V. C., and Lin, C., "Prediction of Turbulent Flow over Rough Surfaces Using a Force Field in Large Eddy Simulation," *Journal of Fluids Engineering*, Vol. 125, No. 1, 2003, pp. 2–9.
doi:10.1115/1.1524587

[9] Bhaganagar, K., Kim, J., and Coleman, G., "Effect of Roughness on Wall-Bounded Turbulence," *Flow, Turbulence and Combustion*, Vol. 72, Nos. 2–4, 2004, pp. 463–492.
doi:10.1023/B:APPL.0000044407.34121.64

[10] Taylor, R. P., Coleman, H. W., and Hodge, B. K., "Prediction of Turbulent Rough-Wall Skin-Friction Using a Discrete Element Approach," *Journal of Fluids Engineering*, Vol. 107, No. 2, 1985, pp. 251–257.

[11] Taylor, R. P., Scaggs, W. F., and Coleman, H. W., "Measurement and Prediction of the Effects of Nonuniform Surface Roughness on Turbulent Flow Friction Coefficients," *Journal of Fluids Engineering*, Vol. 110, No. 3, 1988, pp. 380–384.

[12] Taylor, R. P., Hodge, B. K., and Coleman, H. W., "Discrete Element Model for Turbulent Skin-Friction Prediction for Rib-Type Surface Roughness," *Heat and technology*, Vol. 7, No. 1, 1989, pp. 29–48.

[13] Tarada, F., "Prediction of Rough-Wall Boundary Layers Using a Low Reynolds Number k-ε Model," *International Journal of Heat and Fluid Flow*, Vol. 11, No. 4, 1990, pp. 331–345.
doi:10.1016/0142-727X(90)90057-I

[14] Maruyama, T., "Surface and Inlet Boundary Conditions for the Simulation of Turbulent Boundary Layer over Complex Rough Surfaces," *Journal of Wind Engineering and Industrial Aerodynamics*, Vol. 81, May–July 1999, pp. 311–322.
doi:10.1016/S0167-6105(99)00026-4

[15] Yamamoto, M., "Proposal of a RANS Model to Predict Both k- and d-Type Roughness," *Proceedings of the 4th ASME/JSME Joint Fluids Engineering Conference*, Vol. 1, Pt. C, 2003, pp. 2019–2024.

[16] Krogstad, P.-Å., "Modification of the Van Driest Damping Function to Include the Effects of Surface Roughness," *AIAA Journal*, Vol. 29, No. 6, 1991, pp. 888–894.
doi:10.2514/3.10675

[17] van Driest, E. R., "On Turbulent Flow Near a Wall," *Journal of Aerospace Science*, Vol. 23, No. 11, 1956, pp. 1007–1011.

[18] Youn, B., Yuen, C., and Mills, A. F., "Friction Factor for Flow in Rectangular Ducts with One Side Rib-Roughened," *Journal of Fluids Engineering*, Vol. 116, No. 3, 1994, pp. 488–493.
doi:10.1115/1.2910303

[19] Zhang, H., Faghri, M., and White, F. M., "New Low-Reynolds-Number k-ε Model for Turbulent Flow over Smooth and Rough Surfaces," *Journal of Fluids Engineering*, Vol. 118, No. 2, 1996, pp. 255–259.
doi:10.1115/1.2817371

[20] Lam, C. K. G., and Bremhorst, K., "A Modified Form of the k-ε Model for Predicting Wall Turbulence," *Journal of Fluids Engineering*, Vol. 103, No. 3, 1981, pp. 456–460.

[21] Durbin, P. A., Medic, G., Seo, J.-M., Eaton, J. K., and Song, S., "Rough Wall Modification of Two-Layer k-ε," *Journal of Fluids Engineering*, Vol. 123, No. 1, 2001, pp. 16–21.
doi:10.1115/1.1343086

[22] Chen, H. C., and Patel, V. C., "Near-Wall Turbulence Models for Complex Flows Including Separation," *AIAA Journal*, Vol. 26, No. 6, 1988, pp. 641–648.
doi:10.2514/3.9948

[23] Foti, E., and Scandura, P., "A Low Reynolds Number k-ε Model Validated for Oscillatory Flows over Smooth and Rough Walls," *Coastal Engineering*, Vol. 51, No. 2, 2004, pp. 173–184.
doi:10.1016/j.coastaleng.2004.01.001

[24] Launder, B. E., and Sharma, B. I., "Application of the Energy-Dissipation Model of Turbulence to the Calculation of Flow Near a Spinning Disc," *Letters in Heat and Mass Transfer*, Vol. 1, No. 2, 1974, pp. 131–138.
doi:10.1016/0094-4548(74)90150-7

[25] Mansour, N. N., Kim, J., and Moin, P., "Reynolds Stress and Dissipation Rate Budgets in Turbulent Channel Flow," *Journal of Fluid Mechanics*, Vol. 194, Sept. 1988, pp. 15–44.
doi:10.1017/S0022112088002885

[26] Klebanoff, P. S., "Characteristic of Turbulence in a Boundary Layer with Zero Pressure Gradient," NACA TM-1247, 1954.

[27] Bakken, O. M., Krogstad, P.-Å., Ashrafian, A., and Andersson, H. I., "Reynolds Number Effects in the Outer Layer of the Turbulent Flow in a Channel with Rough Walls," *Physics of Fluids*, Vol. 17, No. 6, 2005, p. 065101.
doi:10.1063/1.1900146

[28] Antonia, R. A., and Krogstad, P.-Å., "Turbulence Structure in Boundary Layers over Different Types of Surface Roughness," *Fluid Dynamics Research*, Vol. 28, No. 2, 2001, pp. 139–157.
doi:10.1016/S0169-5983(00)00025-3

[29] Flack, K. A., Schultz, M. P., and Connelly, J. A., "Examination of a Critical Roughness Height for Outer Layer Similarity," *Physics of Fluids*, Vol. 19, No. 9, 2007, pp. 095104–095109.
doi:10.1063/1.2757708

[30] George, J., and Simpson, R. L., "Transport-Rate Budgets of Reynolds Stresses in 2-D and 3-D Rough-Wall Turbulent Boundary Layers," AIAA Paper 2004–1286, 2004.

[31] Keirsbulck, L., Labraga, L., Mazouz, A., and Tournier, C., "Surface Roughness Effects on Turbulent Boundary Layer Structures," *Journal of Fluids Engineering*, Vol. 124, No. 1, 2002, pp. 127–135.
doi:10.1115/1.1445141

[32] Bergstrom, D. J., Akinlade, O. G., and Tachie, M. F., "Skin Friction Correlation for Smooth and Rough Wall Turbulent Boundary Layers," *Journal of Fluids Engineering*, Vol. 127, No. 6, 2005, pp. 1146–1153.
doi:10.1115/1.2073288

[33] Wang, H., and Takle, E. S., "Boundary-Layer Flow and Turbulence Near Porous Obstacles 1: Derivation of a General Equation Set for a Porous Medium," *Boundary-Layer Meteorology*, Vol. 74, Nos. 1–2, 1995, pp. 73–88.
doi:10.1007/BF00715711

[34] Antohe, B. V., and Lage, J. L., "A General Two-Equation Macroscopic Turbulence Model for Incompressible Flow in Porous Media," *International Journal of Heat and Mass Transfer*, Vol. 40, No. 13, 1997, pp. 3013–3024.
doi:10.1016/S0017-9310(96)00370-5

[35] Getachew, D., Minkowycz, W. J., and Lage, J. L., "Modified Form of the k-ε Model for Turbulent Flows of an Incompressible Fluid in Porous Media," *International Journal of Heat and Mass Transfer*, Vol. 43, No. 16, 2000, pp. 2909–2915.
doi:10.1016/S0017-9310(99)00345-2

[36] Pedras, M. H. J., and de Lemos, M. J. S., "Macroscopic Turbulence Modeling for Incompressible Flow Through Undeformable Porous Media," *International Journal of Heat and Mass Transfer*, Vol. 44, No. 6, 2001, pp. 1081–1093.
doi:10.1016/S0017-9310(00)00202-7

[37] Silva, R. A., and de Lemos, M. J. S., "Turbulent Flow in a Channel Occupied by a Porous Layer Considering the Stress Jump at the Interface," *International Journal of Heat and Mass Transfer*, Vol. 46, No. 26, 2003, pp. 5113–5121.
doi:10.1016/S0017-9310(03)00368-5

[38] Breugem, W. P., "The Influence of Wall Permeability on Laminar and Turbulent Flows," Ph.D. Dissertation, Technische Univ. Delft, Delft, The Netherlands, 2004.

[39] de Lemos, M. J. S., and Silva, R. A., "Turbulent Flow over a Layer of a Highly Permeable Medium Simulated with a Diffusion-Jump Model for the Interface," *International Journal of Heat and Mass Transfer*, Vol. 49, Nos. 3–4, 2006, pp. 546–556.
doi:10.1016/j.ijheatmasstransfer.2005.08.028

[40] Ochoa-Tapia, J. A., and Whitaker, S., "Momentum Transfer at the Boundary Between a Porous Medium and a Homogeneous Fluid, 1: Theoretical Development," *International Journal of Heat and Mass Transfer*, Vol. 38, No. 14, 1995, pp. 2635–2646.
doi:10.1016/0017-9310(94)00346-W

[41] Ochoa-Tapia, J. A., and Whitaker, S., "Momentum Transfer at the Boundary Between a Porous Medium and a Homogeneous Fluid, 2: Comparison with Experiment," *International Journal of Heat and Mass Transfer*, Vol. 38, No. 14, 1995, pp. 2647–2655.
doi:10.1016/0017-9310(94)00347-X

[42] Brinkman, H. C., "A Calculation of the Viscous Force Exerted by a Flowing Fluid on a Dense Swarm of Particles," *Applied Scientific Research*, Vol. A1, 1948, p. 27.

[43] Koplik, J., Levine, H., and Zee, A., "Viscosity Renormalization in the Brinkman Equation," *Physics of Fluids*, Vol. 26, No. 10, 1983, pp. 2864–2870.
doi:10.1063/1.864050

[44] Kaviany, M., "Laminar Flow Through a Porous Channel Bounded by Isothermal Parallel Plates," *International Journal of Heat and Mass Transfer*, Vol. 28, No. 4, 1985, pp. 851–858.
doi:10.1016/0017-9310(85)90234-0

[45] Durlofsky, L., and Brady, J. F., "Analysis of the Brinkman Equation as a Model for Flow in Porous Media," *Physics of Fluids*, Vol. 30, No. 11, 1987, pp. 3329–3341.

doi:10.1063/1.866465
[46] Renken, K. J., and Carneiro, M. J., "Effect of Forced Convection on Enhanced Film Condensation Within Thin Porous Coatings," *American Society of Mechanical Engineers Winter Annual Meeting*, Vol. 216, American Society of Mechanical Engineers, New York, 1992, pp. 27–34.
[47] Goyeau, B., Songbe, J.-P., and Gobin, D., "Numerical Study of Double-Diffusive Natural Convection in a Porous Cavity Using the Darcy-Brinkman Formulation," *International Journal of Heat and Mass Transfer*, Vol. 39, No. 7, 1996, pp. 1363–1378.
doi:10.1016/0017-9310(95)00225-1
[48] Kuznetsov, A. V., and Xiong, M., "Numerical Simulation of the Effect of Thermal Dispersion on Forced Convection in a Circular Duct Partly Filled with a Brinkman-Forchheimer Porous Medium," *International Journal of Numerical Methods for Heat and Fluid Flow*, Vol. 10, No. 5, 2000, pp. 488–501.
doi:10.1108/09615530010338169
[49] Martys, N. S., "Improved Approximation of the Brinkman Equation Using a Lattice Boltzmann Method," *Physics of Fluids*, Vol. 13, No. 6, 2001, pp. 1807–1810.
doi:10.1063/1.1368846
[50] Parvazinia, M., Nassehi, V., Wakeman, R. J., and Ghoreishy, M. H. R., "Finite Element Modelling of Flow Through a Porous Medium Between Two Parallel Plates Using the Brinkman Equation," *Transport in Porous Media*, Vol. 63, No. 1, 2006, pp. 71–90.
doi:10.1007/s11242-005-2721-2
[51] Beavers, G. S., and Joseph, D. D., "Boundary Conditions at a Naturally Permeable Wall," *Journal of Fluid Mechanics*, Vol. 30, No. 1, 1967, pp. 197–207.
doi:10.1017/S0022112067001375
[52] Chellaiah, S., and Viskanta, R., "Freezing of Water-Saturated Porous Media in the Presence of Natural Convection: Experiments and Analysis," *Journal of Heat Transfer*, Vol. 111, No. 2, 1989, pp. 425–432.
[53] Kladias, N., and Prasad, V., "Experimental Verification of Darcy-Brinkman-Forchheimer Flow Model for Natural Convection in Porous Media," *Journal of Thermophysics and Heat Transfer*, Vol. 5, No. 4, 1991, pp. 560–576.
doi:10.2514/3.301
[54] Zhong, W. H., Currie, I. G., and James, D. F., "Creeping Flow Through a Model Fibrous Porous Medium," *Experiments in Fluids*, Vol. 40, No. 1, 2006, pp. 119–126.
doi:10.1007/s00348-005-0053-1
[55] Scheidegger, A. E., *The Physics of Flow Through Porous Media*, Univ. of Toronto Press, Toronto, 1974.
[56] Shukla, J. B., "A New Theory of Lubrication for Roughness," *Wear*, Vol. 49, No. 1, 1978, pp. 33–42.
doi:10.1016/0043-1648(78)90021-2
[57] Tichy, J. A., "Porous Media Model for Thin Film Lubrication," *Journal of Tribology*, Vol. 117, No. 1, 1995, pp. 16–21.
doi:10.1115/1.2830595
[58] Whitaker, S., *The Method of Volume Averaging*, Kluwer, Dordrecht, The Netherlands, 1999.
[59] Pedras, M. H. J., and de Lemos, M. J. S., "On the Definition of Turbulent Kinetic Energy for Flow in Porous Media," *International Communications in Heat and Mass Transfer*, Vol. 27, No. 2, 2000, pp. 211–220.
doi:10.1016/S0735-1933(00)00102-0
[60] Whitaker, S., "Forchheimer Equation: A Theoretical Development," *Transport in Porous Media*, Vol. 25, No. 1, 1996, pp. 27–61.
doi:10.1007/BF00141261
[61] Lu, M., and Liou, W. W., "Assessment of Two Low-Reynolds-Number k-ε Models in Turbulent Boundary Layers with Surface Roughness," *Journal of Spacecraft and Rockets*, Vol. 44, No. 6, 2007, pp. 1307–1316.
doi:10.2514/1.30738
[62] Sinha, S. K., Sotiropouslos, F., and Odgaard, A. J., "Three-Dimensional Numerical Model for Flows Through Natural Rivers," *Journal of Hydraulic Engineering*, Vol. 124, No. 1, 1998, pp. 13–24.
doi:10.1061/(ASCE)0733-9429(1998)124:1(13)
[63] Lu, M., and Sirviente, A. I., "Numerical Study of the Momentumless Wake of an Axisymmetric Body," *43rd AIAA Aerospace Sciences Meeting and Exhibit*, AIAA, Reston, VA, 2005, pp. 10175–10188.
[64] Kim, K., Sirviente, A. I., and Beck, R. F., "The Complementary RANS Equations for the Simulation of Viscous Flows," *International Journal for Numerical Methods in Fluids*, Vol. 48, No. 2, 2005, pp. 199–229.
doi:10.1002/fld.892
[65] Prandtl, L., and Schlichting, H., "Das Wiederstandagesetz Rouher Platten," *Werft-Reederei-Hafen*, Vol. 15, 1934, pp. 1–4.

P. Givi
Associate Editor